

Thermodynamics of Meissner effect and flux pinning behavior in the bulk of single-crystal $\text{La}_{2-x}\text{Sr}_x\text{CuO}_4$ ($x=0.09$)

I. Dhiman,^{1,2,*} R. Ziesche,^{2,3} V. K. Anand,² L. Riik,^{2,4} Gian Song,¹ A. T. M. N. Islam,² Isao Tanaka,⁵ and W. Treimer^{2,4}

¹Chemical and Engineering Materials Division, Oak Ridge National Laboratory, Oak Ridge, Tennessee 37831, USA

²Helmholtz-Zentrum Berlin für Materialien und Energie GmbH, Hahn-Meiter Platz 1, D-14109 Berlin, Germany

³Department of Chemical Engineering, University College London, Torrington Place, London WC1E 7JE, United Kingdom

⁴University of Applied Sciences, Beuth Hochschule für Technik Berlin, D-13353 Berlin, Germany

⁵Center for Crystal Science and Technology, University of Yamanashi, 7-32 Miyamae, Kofu, Yamanashi 4008511, Japan

(Received 20 April 2017; revised manuscript received 7 September 2017; published 28 September 2017)

We have studied the evolution of magnetic flux pinning behavior in the Meissner phase and the mixed state for the high- T_c single-crystal $\text{La}_{2-x}\text{Sr}_x\text{CuO}_4$ ($x = 0.09$) superconductor using the polarized neutron imaging method with varying magnetic field and temperature. In the Meissner state expulsion of magnetic field (switched on during the measurements) is visualized, and the signatures of a mixed state with increasing temperature are observed. However, for flux pinning behavior in the range $5 \text{ K} \leq T \leq 15 \text{ K}$ and $H_{\text{ext}} = 63.5 \text{ mT}$ (switched off during the measurements), the evolution of the fringe pattern indicates magnetic flux pinning inside the bulk of the sample. At $25 \text{ K} \leq T \leq 32 \text{ K}$, a continuous decrease in inhomogeneously distributed pinned magnetic flux is observed, with the sample reaching a normal conducting state at T_c ($\approx 32 \text{ K}$). The flux pinning behavior is also explored as a function of H_{ext} at $T = 5 \text{ K}$. As expected, with increasing H_{ext} an increase in fringe density is observed, indicating an increase in magnetic flux pinning in the bulk of the sample. A comparison between calculated and experimentally visualized pinned magnetic fluxes shows good agreement. This implies quantification of pinned magnetic flux inside the sample, which is not possible with any other technique for bulk samples.

DOI: [10.1103/PhysRevB.96.104517](https://doi.org/10.1103/PhysRevB.96.104517)

I. INTRODUCTION

Since the discovery of high- T_c superconductivity in doped cuprates, the nature and understanding of superconductivity in these materials have been the subject of substantial interest, owing to their intriguing properties and high transition temperatures T_c [1–8]. $\text{La}_{2-x}\text{Sr}_x\text{CuO}_4$ is one such high- T_c superconductor, a prototype material for investigations and understanding of superconductivity in the family of cuprates [1,7,9–11]. The $\text{La}_{2-x}\text{Sr}_x\text{CuO}_4$ series exhibits several thermodynamic phases depending on the degree of doping and oxygen content. The stoichiometric undoped parent compound La_2CuO_4 is an antiferromagnetic insulator with a Néel temperature $T_N \approx 320 \text{ K}$ for the ordering of Cu^{2+} moments [12]. Substituting divalent Sr with trivalent La or the presence of excess oxygen leads to hole doping, causing suppression of long-range-ordered antiferromagnetism [13–19]. A nominal substitution of 2% Sr ($x = 0.02$) completely suppresses the antiferromagnetic ordering in $\text{La}_{2-x}\text{Sr}_x\text{CuO}_4$ [19,20], whereas a superconducting state appears at $x \geq 0.055$ with a maximum T_c for $x = 0.15$. With type-II behavior these high- T_c superconductors present an intriguing vortex phase [21–25].

Understanding the flux pinning behavior is important not only from the viewpoint of physics but also from a technological standpoint, as this is the mechanism involved in enhancing critical current values in type-II superconductors [26–31]. For most applications it is extremely desirable to control pinning effects and the related current densities. To

obtain insight into the mixed-state flux pinning behavior and the complex interplay of superconductivity with magnetism in these systems, several studies, in particular neutron-scattering-based measurements [32–47] in reciprocal space and various surface-based imaging techniques in real space, have been performed. The vortex lattice structures in superconductors are also investigated with the small-angle neutron scattering (SANS) technique [48–53]. However, the neutron scattering is averaged through the whole sample, and the details of the inhomogeneous vortex lattice structures have not been resolved.

The surface-based scanning tunneling microscopy (STM) technique has been extensively used to study superconducting vortices, particularly for the high- T_c $\text{Bi}_2\text{Sr}_2\text{CaCu}_2\text{O}_{8+\delta}$ and $\text{YBa}_2\text{Cu}_3\text{O}_7$ cuprates [54–59]. The major challenge with STM is to have atomically flat and stable and extremely clean surfaces. Another technique utilized for the visualization of magnetic flux distribution is magneto-optical imaging [56,60–63]. In this method the local supercurrent density distribution is mapped in thin superconducting films, with out-of-plane component sensitivity and spatial resolution of the order of $5 \mu\text{m}$. Further, techniques based on scanning superconducting quantum interference devices (SQUIDS) [56,64], time-resolved Lorentz microscopy imaging [65–69], magnetic force, and scanning Hall probe microscopy ([56] and references therein) have also been used to study the interactions, flux lattice dynamics, and geometries of vortices in multiband superconductors. These techniques indeed provide high-resolution images; however, the information obtained stems from rather two-dimensional objects, providing insight into superconducting mixed states on the surface.

The polarized neutron imaging technique, on the other hand, provides a unique probe for the visualization of the

*idhiman@ornl.gov

magnetic field in and around the bulk of a sample, therefore making a substantial contribution to the field of superconductivity and magnetism [70]. Flux pinning in $\text{La}_{2-x}\text{Sr}_x\text{CuO}_4$ systems has previously been investigated by Kishio *et al.* [71] for $x = 0.065$ and 0.07 using magnetization measurements. However, in this technique one has to deal with the undesirable demagnetization effects. In contrast, with the polarized neutron imaging technique flux pinning behavior can be visualized in the bulk samples; therefore the demagnetization effect does not have any direct bearing on the flux pinning behavior. Furthermore, with the magnetization measurement technique one cannot visualize magnetic field expulsion or flux pinning in real space. The polarized neutron imaging technique makes this visualization possible.

In the current study, we are interested in investigating and understanding the complex interplay of the flux pinning phenomenon and Meissner behavior in the mixed state as a function of temperature and externally applied magnetic field H_{ext} in the bulk of an underdoped $\text{La}_{2-x}\text{Sr}_x\text{CuO}_4$ ($x = 0.09$) single-crystal sample using a real-space polarized neutron imaging technique. In addition, the real-space visualization of magnetic domain structures has been so far limited to surface-sensitive techniques. However, neutrons can easily penetrate bulk samples and, due to their magnetic moment, can interact with the local magnetic field distributions. Recently, this technique has been recognized as a powerful nondestructive tool to visualize the magnetic field distribution in various ferromagnetic samples and pinned flux in superconductors [72–77]. From a macroscopic viewpoint, the superconducting state is a thermodynamic phase. Involving temperature and magnetic field as an external variable is an effective way to understand the evolution of flux pinning behavior in bulk samples.

II. THEORETICAL CONSIDERATION

Visualization of the magnetic field using polarized neutrons is based on the neutron spin interaction with the magnetic field in the bulk samples. The neutron spin interacts with the magnetic field B (in and around the sample), rotating around B with a Larmor frequency $\omega_L = \gamma_L B$, where $\gamma_L = g\mu_N\hbar = -1.832 \times 10^8 \text{ rad s}^{-1} \text{ T}^{-1}$ is the gyromagnetic ratio of the neutron, $\mu_N = 5.5078 \times 10^{-27} \text{ J/T}$ is the nuclear magneton, $g = -3.8261$ is the Landé factor for neutrons, and \hbar ($\hbar = \frac{h}{2\pi}$) is the Planck constant. If the neutron spin interacts with a magnetic field B which is not parallel or antiparallel to its spin direction, it begins to undergo Larmor precession with the frequency ω_L . The rotation angle ϕ of the neutron spin is dependent on the time t taken by the neutrons to pass through the magnetic field. The ϕ can be calculated as

$$\phi = \omega_L t = \gamma_L B t = \frac{\gamma_L}{v} \int_{\text{path}} \vec{B} \cdot d\vec{s} = \frac{\gamma_L \lambda m}{h} B s, \quad (1)$$

where m is the neutron mass, s is the path integral in the field, v ($= \frac{h}{m\lambda}$) is the neutron velocity, and λ is the wavelength. The integration limit for pinned flux is defined by sample dimensions and is dependent on the amount of magnetic field B .

III. EXPERIMENTAL DETAILS

Single-crystal growth of $\text{La}_{2-x}\text{Sr}_x\text{CuO}_4$ ($x = 0.09$) was carried out in a four-mirror-type optical image furnace (Crystal Systems Corp., Japan) using the traveling-solvent-floating-zone technique. We used oriented crystal as a seed rod, which enabled epitaxial growth of the crystal along the [010] direction. In this way we were able to obtain an oriented crystal of almost cylindrical geometry with the cylindrical axis along the crystallographic [010] direction. The composition of the single crystal was determined by electron-probe microanalysis (EPMA) using a standard sample. X-ray Laue diffraction was used to check the quality of the as-grown single crystal and to orient the crystal along the particular crystallographic direction. The magnetic susceptibility measurements were performed using a Quantum Design SQUID vibration sample magnetometer (SQUID-VSM) at the Mag Lab, Helmholtz-Zentrum Berlin.

The polarized neutron imaging measurements were performed on the instrument PONTO II (polarized neutron tomography) located at BER II (Berlin research reactor) of the Helmholtz-Zentrum Berlin für Materialien und Energie, in the neutron guide hall at the NL1a beam port. It is dedicated for radiography and tomography studies using polarized neutrons, covering a wavelength range of $0.29 \text{ nm} < \lambda < 0.45 \text{ nm}$ using a graphite monochromator [(002), reflection]. A detailed description of the instrument can be found in Ref. [78]. For the present study, the graphite monochromator was positioned to reflect a mean wavelength of $0.32(1) \text{ nm}$ towards an optical bench. Soller collimators were utilized for both horizontal and vertical collimation of the beam with 0.1° divergence. For beam polarization (spin analysis) a bender-type polarizer (analyzer) was used, providing a polarization degree of $P = 92\%$. Neutron flux at the sample position was $3.2 \times 10^6 \text{ neutrons cm}^{-2} \text{ s}^{-1}$, with a field of view of $40 \times 40 \text{ mm}^2$, and the obtained two-dimensional spatial resolution for polarized neutrons was $130 \mu\text{m}$. The detector unit comprised a LiZnS scintillator, Nikon objective, and Andor CCD camera with a pixel array of $2k \times 2k$ (each pixel size = $13.6 \mu\text{m} \times 13.6 \mu\text{m}$). The sample was placed in an aluminum sample holder, which was screwed to the cold finger of a closed-cycle refrigerator and could be rotated by 360° ($\pm 0.005^\circ$). A homogeneous external magnetic field H_{ext} was applied using a pair of Helmholtz coils at the sample position. The exposure time for each radiograph was 2 h.

With polarized neutron imaging, the measured transmission intensity is a sum of the contribution from the interaction of the neutron spin with the sample magnetic field, the conventional attenuation (depending on sample composition and density), and scattering. To remove the conventional attenuation and scattering contribution, radiographs were normalized with respect to the radiographs measured with no magnetic contribution in the normal conducting state for $T > T_c$. This is particularly important for small magnetic field contributions. All the neutron radiographs recorded were corrected for dark field and the constant background and electronic noise from the detector and normalized with respect to the radiographs recorded at 50 K, above T_c ($\approx 31.65 \text{ K}$).

The sample was approximately cylindrical in shape with dimensions of a radius of 2.4 mm and a height of 5.8 mm.

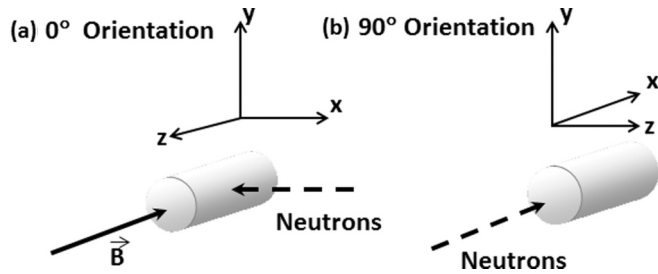


FIG. 1. Sample orientation with respect to the incident neutrons, wherein (a) for a 0° orientation the sample axis is perpendicular to the incident neutrons, while (b) for a 90° orientation the sample axis is parallel to the incident neutrons. To visualize flux pinning behavior in the 90° orientation, first, the sample is cooled down to 5 K with $H_{\text{ext}} = 63.5$ mT along the direction parallel to the sample axis, i.e., in the 0° position. Thereafter, H_{ext} is switched off, and the sample is turned to the 90° position.

To visualize the flux pinning behavior, field cooling (FC) was employed. First, the sample was cooled to 50 K in one step. After a waiting time of nearly 1 h, 2-h polarized neutron radiography measurements were performed at $T = 50$ K ($T > T_c$). After this a homogeneous external magnetic field H_{ext} was applied, and the sample was cooled down to 5 K. At 5 K, the external magnetic field ($H_{\text{ext}} = 0$) was switched off to investigate the flux pinning behavior. Now, again radiographs were recorded at various temperature steps up to 32 K, just above T_c . For all the measurements reported here the external magnetic field was applied along the 0° orientation, i.e., for sample axis orientation parallel to the external magnetic field (as shown in Fig. 1). However, for the visualization of the Meissner effect the sample was zero field cooled to 5 K. Thereafter, magnetic field was switched on, and radiographs were measured in steps while warming the sample from 5 to 32 K ($T > T_c$).

IV. RESULTS AND DISCUSSION

A. Magnetization behavior

To determine T_c for the $\text{La}_{2-x}\text{Sr}_x\text{CuO}_4$ ($x = 0.09$) sample, magnetization measurements as a function of temperature were carried out. The temperature-dependent volumetric magnetic susceptibility plots are shown in Fig. 2. The temperature-dependent magnetization data are obtained with zero-field-cooled warming of the sample in the presence of external magnetic field ($H_{\text{ext}} = 20$ and 50 mT). The superconducting transition temperature for the $\text{La}_{2-x}\text{Sr}_x\text{CuO}_4$ ($x = 0.09$) sample is ≈ 32.05 K for $H_{\text{ext}} = 20$ mT. Below this temperature, the sample displays a Meissner response, with a strong diamagnetic signal. A small decrease in critical temperature T_c ($=31.65$ K) is observed on increasing H_{ext} to 50 mT. An indirect estimate of the superconducting phase fraction is obtained from the magnetization data. The demagnetization factor for perfect cylindrical geometry has been taken into consideration to estimate the superconducting volume fraction [79]. The obtained volumetric fraction is nearly 100% for 20 mT at $T = 5$ K. As expected, this value is reduced to $\approx 91\%$ for a higher magnetic field of 50 mT. However, with magnetization measurements no information about the flux

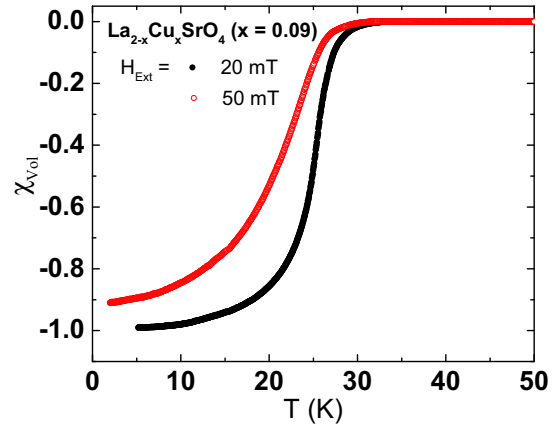


FIG. 2. Volumetric magnetic susceptibility as a function of temperature at $H_{\text{ext}} = 20$ mT (solid circles) and 50 mT (open circles) for the $\text{La}_{2-x}\text{Sr}_x\text{CuO}_4$ ($x = 0.09$) single-crystal sample.

pinning behavior can be obtained in the bulk of the sample. The magnetization behavior is in agreement with that reported for the $\text{La}_{2-x}\text{Sr}_x\text{CuO}_4$ series in the literature [14].

Based on these initial magnetization results, the polarized neutron imaging measurements as a function of temperature were carried out on cylindrical shaped $\text{La}_{2-x}\text{Sr}_x\text{CuO}_4$ ($x = 0.09$) single-crystal sample. In the Meissner phase (for $T < T_c$), the expelled magnetic field is visualized as the superposition of expelled magnetic field and H_{ext} . On the other hand, flux pinning behavior leads to an evolution of the pinned flux lines and pattern inside the sample, as discussed in greater detail below. Assuming that the polarizer and analyzer are configured for spin-up neutrons and for strong enough magnetic field of the sample, the outgoing neutron spin is rotated, i.e., makes a π flip. This would cause the minimum transmission (for the ideal setup) intensity measured on the detector placed behind the analyzer. Now if the analyzer is modified to accept only spin-down neutrons (π flip), inversion in the transmission intensity contrast, i.e., the maximum transmission, is measured on the detector. All the other neutron spin precession values between zero and π will lead to gray-value contrast, depending on the total degree of polarization and instrument resolution. Representative radiographs exhibiting the flux pinning behavior below T_c are shown in Fig. 3. The two radiographs shown are recorded with spin-up and -down incident neutrons, causing change in contrast (bright to dark).

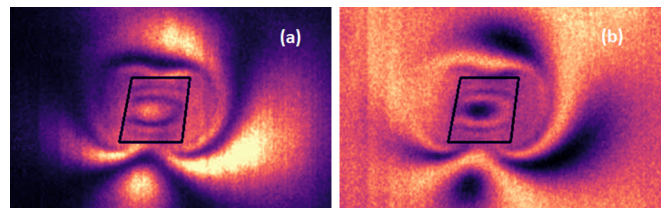


FIG. 3. Representative radiographs for the single-crystal $\text{La}_{2-x}\text{Sr}_x\text{CuO}_4$ ($x = 0.09$) sample at 5 K and $H_{\text{ext}} = 30$ mT for the 0° orientation, depicting the fringe patterns with (a) spin-down (dark) and (b) spin-up (bright) neutrons. The black box indicates the sample cross section.

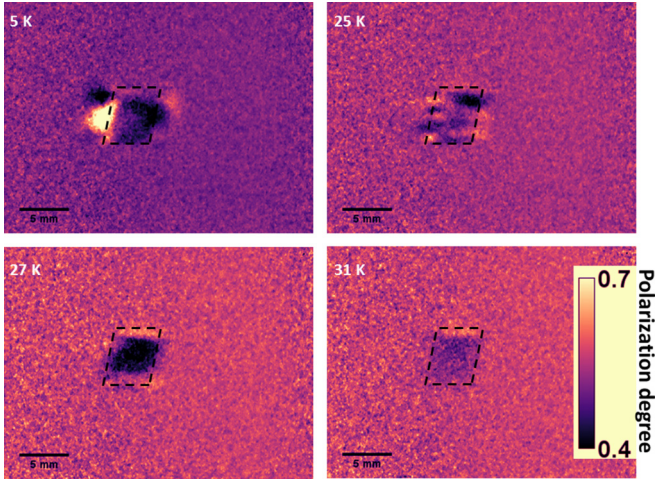


FIG. 4. Meissner effect as a function of temperature at $H_{\text{ext}} = 10$ mT for the single-crystal $\text{La}_{2-x}\text{Sr}_x\text{CuO}_4$ ($x = 0.09$) sample below T_c . For these measurements, the sample is cooled down to 5 K from room temperature with $H_{\text{ext}} = 0$ mT. At 5 K, to visualize the Meissner effect, H_{ext} is set to 10 mT. The black dashed box indicates the sample, and the scale bar is 5 mm.

The alteration of fringe pattern intensity from dark to bright corresponds to a spin rotation of π (π flip), implying the magnetic nature of these fringes. Each individual fringe in the figure indicates that all the incoming polarized neutrons experience the same path integral ($\int_{\text{path}} \mathbf{B} \cdot d\mathbf{s}$) change.

B. Meissner effect

In Fig. 4, neutron radiographs show the temperature dependence of the Meissner effect in the presence of external magnetic field. The sample is cooled down to 5 K below T_c , with $H_{\text{ext}} = 0$ mT. Then the magnetic field is applied to the sample. As observed in Fig. 4 for $T < T_c$ at $H_{\text{ext}} = 10$ mT, a dark pattern appears around the sample, indicating expulsion of magnetic field. As a function of increasing temperature, a weak signature of the mixed state is observed, wherein the expelled magnetic flux begins to penetrate, in agreement with the change in transmission contrast inside (dark pattern) and outside (bright pattern) the sample. This contrast indicates the difference in magnitude of the stray field in and around the sample. At 27 K, the bright pattern outside the sample is reduced, indicating the weakening of the Meissner effect. On further increasing the temperature $T \geq T_c$, the pattern disappears with the sample reaching a normal state. Therefore one recognizes the evolution of the mixed state, with changes in pinned and expelled magnetic flux in and around the sample, as a function of temperature.

C. Flux pinning behavior as a function of temperature

In a normal nonsuperconducting state for $T > T_c$, applied magnetic field penetrates the whole sample. Now when the sample is field cooled below T_c , this applied field is expected to be expelled. At 5 K, with H_{ext} switched off no magnetic contrast is expected inside the sample. In contrast, in the present study the fringe pattern is evolved for $T < T_c$ at 5 K for a $\text{La}_{2-x}\text{Sr}_x\text{CuO}_4$ ($x = 0.09$) single-crystal sample.

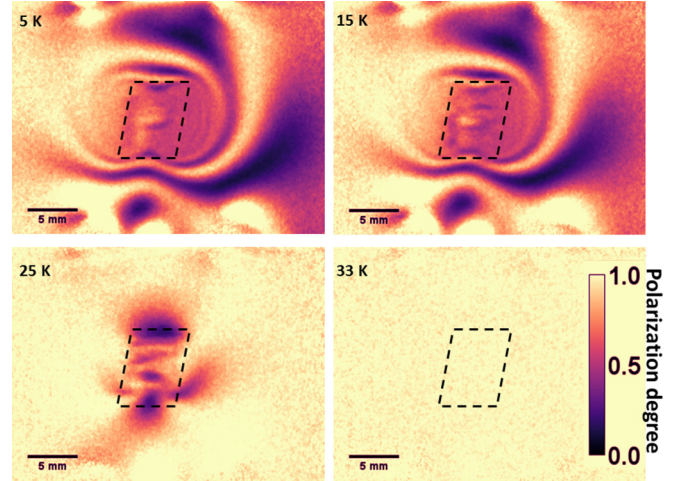


FIG. 5. Temperature dependence of flux pinning behavior at $H_{\text{ext}} = 63.5$ mT for the 0° orientation for the single-crystal $\text{La}_{2-x}\text{Sr}_x\text{CuO}_4$ ($x = 0.09$) sample. Towards these measurements, the sample is cooled down to 5 K from room temperature in the presence of H_{ext} . Thereafter, to visualize flux pinning, the external magnetic field is switched off. Consequently, any depolarization of neutron spin can be attributed to the flux pinned within the sample. The black dashed box indicates the sample, and the scale bar is 5 mm.

Figure 5 shows the measured radiographs in the 0° orientation [see Fig. 1(a)] for $\text{La}_{2-x}\text{Sr}_x\text{CuO}_4$ ($x = 0.09$) single-crystal sample as a function of temperature, exhibiting a signature of the flux pinning behavior. For these measurements, the sample is cooled down to 5 K in the presence of external magnetic field ($H_{\text{ext}} = 63.5$ mT). Thereafter, H_{ext} is switched off. Any change in incident neutron spin rotation must be attributable to the flux pinned in the sample. Consequently, the temperature-dependent behavior in the present study is entirely a sample phenomenon. In Fig. 5, evolution of the closed-loop-type (outside the sample) fringe pattern at $T = 5$ and 15 K is observed. The appearance of this fringe pattern for $T < T_c$ clearly indicates the flux pinning behavior inside the sample. Also, for $T = 5$ and 15 K fringes located close to the longitudinal axis appear higher in intensity (Fig. 5) and diminish on moving towards the sample edge. This behavior implies maximum neutron spin precession around the longitudinal axis. This in turn indicates that the magnetic flux is concentrated around that axis and decreases on moving towards the edge. This effect is further enhanced due to different neutron path lengths through the cylindrical shaped sample. This behavior is in agreement with our previously reported studies on a type-I Pb superconductor [76,77]. This distribution can occur only for a magnetic field which appears to be squeezed around the rod axis; that is, it has a Gaussian-like distribution inside the sample. Detailed calculations pertaining to this can be found in Ref. [76]. At $T = 25$ K, deviation from this Gaussian distribution is observed, and concentration fluctuations in the flux pinning behavior at temperatures close to T_c are ascertained. This deviation is visualized more clearly for the 90° sample orientation in Fig. 7 below. To graphically visualize the effect of temperature, line plots as a function of temperature are presented in Fig. 6. Towards this end, a vertical line is drawn in each radiograph

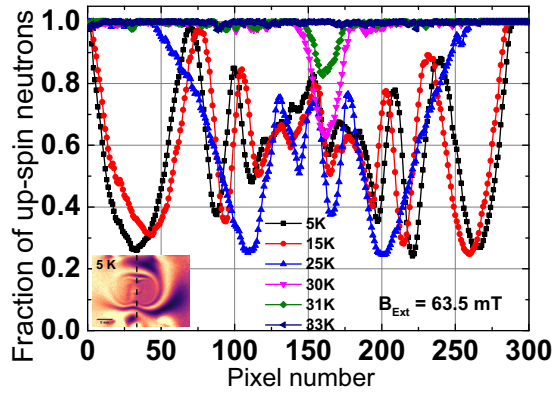


FIG. 6. Line plots to depict the temperature dependence of flux pinning behavior from 5 to 33 K for the single-crystal $\text{La}_{2-x}\text{Sr}_x\text{CuO}_4$ ($x = 0.09$) sample in the 0° orientation, $H_{\text{ext}} = 63.5 \text{ mT}$. The inset radiograph shows an example of the vertical line used for the plot. Each pixel number corresponds to $78 \mu\text{m}$.

where the fringe pattern is quite horizontal, as shown in the inset to Fig. 6. The same procedure is repeated for all the radiographs. With varying temperature a clear reduction in intensity is evidenced above $T = 25 \text{ K}$, in agreement with the reduction in pinned magnetic field as a function of temperature. This behavior indicates strong temperature dependence of pinned flux inside the sample above 25 K.

Figure 7 shows the temperature dependence of flux pinning behavior in the 90° orientation for the $\text{La}_{2-x}\text{Sr}_x\text{CuO}_4$ ($x = 0.09$) single crystal. At 5 K to visualize the flux pinning behavior in the 90° sample orientation, H_{ext} is switched off, and the sample is turned to the 90° position, as shown in Fig. 1. A ring-shaped fringe pattern is observed at $T = 5 \text{ K}$, as depicted in Fig. 7. This is in agreement with the observed striped fringe pattern in the 0° orientation. Collective visualization of this expected behavior in the 0° and 90° orientations can clearly be seen on comparison with the modeled magnetic field distribution in three dimensions for the cylindrical shaped sample described by Treimer *et al.* [76]. The temperature evolution of the flux pinning in the 90° sample orientation exhibits behavior similar to that described for the 0° orientation. In particular, the radiograph measured at 25 K exhibits an inhomogeneous flux distribution, with parts in the sample where flux lines are closer to each other (more concentrated) than in other regions. This behavior indicates deviation from the Gaussian distribution and fluctuations in pinned flux on increasing the temperature close to T_c .

The evolution of the fringe pattern with varying temperature below the critical temperature can be argued to arise from two possibilities: One possibility is the redistribution of pinned magnetic flux within the sample, implying that the amount of pinned magnetic field within the sample is constant; only its distribution is modified on varying the temperature. This behavior would cause a similar fringe pattern, as described for a cylindrical (solenoid) coil in [76]. Another possibility could be the reduction in pinned magnetic flux as a function of temperature. This keeps the shape of the fringe pattern unchanged, and only H_{trap} decreases. On increasing the temperature from 5 to 15 K as shown in Fig. 5 and in the corresponding line plots in Fig. 6, no significant change

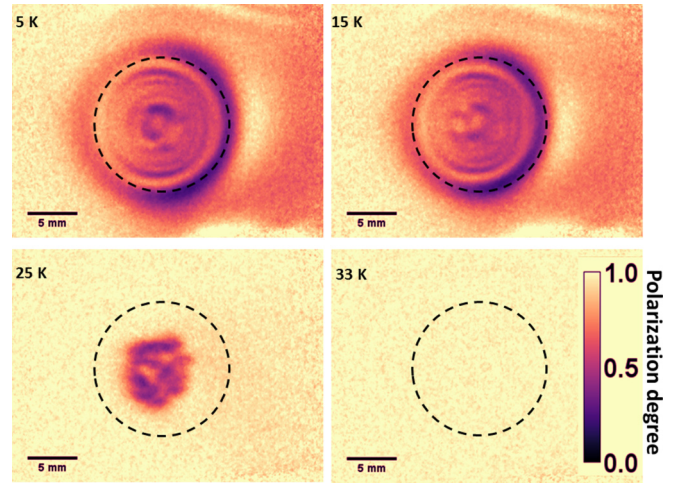


FIG. 7. Flux pinning behavior as a function of temperature for the 90° sample orientation for the single-crystal $\text{La}_{2-x}\text{Sr}_x\text{CuO}_4$ ($x = 0.09$) sample. For these measurements, the sample is cooled down to 5 K with $H_{\text{ext}} = 63.5 \text{ mT}$ applied in the 0° position. At 5 K to visualize the flux pinning behavior for the 90° sample orientation, first, H_{ext} is switched off, and then the sample is turned to the 90° position. The black dashed circle indicates the sample, and the scale bar is 5 mm. Note the decrease in pinned flux with increasing temperature.

in the radiographs is evidenced, indicating that the amount of pinned field is constant up to $T = 15 \text{ K}$. At temperatures between $T = 25$ and 31 K (just below T_c), a drastic change in the magnetic flux fringe pattern indicates a loss of field inside the sample. On warming up the sample above T_c to $T = 32 \text{ K}$, the fringe pattern disappears completely, and the sample reaches a normal nonsuperconducting state.

D. Flux pinning behavior as a function of magnetic field

We further explore the flux pinning behavior as a function of externally applied magnetic field at $T = 5 \text{ K}$. A procedure similar to that described above is employed for these measurements with $H_{\text{ext}} = 10, 20, \text{ and } 30 \text{ mT}$. Figure 8 shows the measured radiographs as a function of field in the 0° sample orientation. As a function of applied magnetic field, the evolution of the fringe pattern is observed. At higher magnetic field the fringe density increases, retaining the Gaussian-shaped distribution of the field inside the sample. As expected, with increasing H_{ext} the number of flux lines pinning the sample also increases. Similar behavior is observed for the 90° sample orientation. The observation of Gaussian flux distribution inside the sample is in contrast to the critical-state Bean model [5]. When the sample is cooled from above T_c in the presence of H_{ext} , the strong pinning centers trap the magnetic flux inside the sample in the normal state in the form of vortices with uniform flux distribution inside the sample. This distribution of vortices is determined by the balance between the Lorentz force of the screening supercurrent and the forces pinning the vortices to material defects and inhomogeneities. The Lorentz force drives these vortices toward the center of the sample, with their motion hindered by the pinning sites. If the external field is varied, the vortices leave or enter the superconductor through its boundary. Additionally, within the region where

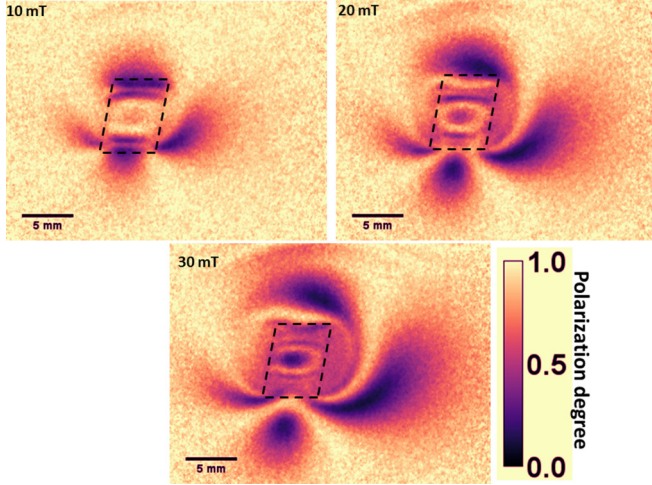


FIG. 8. Flux pinning behavior as a function of external magnetic field at $T = 5$ K for the 0° orientation for the single-crystal $\text{La}_{2-x}\text{Sr}_x\text{CuO}_4$ ($x = 0.09$) sample. Towards this end, the sample is cooled down to 5 K from room temperature, with applied magnetic field. At 5 K, to visualize flux pinning, H_{ext} is switched off. The black dashed box indicates the sample, and the scale bar is 5 mm.

the driving forces are able to surmount the pinning forces, the vortices rearrange themselves into another metastable state, with reestablishment of the equilibrium at the boundary with respect to the external magnetic field.

These experimentally obtained radiographs in the 0° sample orientation as a function of external magnetic field are compared with theoretically modeled magnetic field distribution (simulated ones) to analyze and correlate the neutron spin precession through the magnetic field in the sample. Engel-Herbert and Hesjedal describe the magnetic stray field calculation for a rectangular-shaped bar magnet [80]. In the present study we extend this formalism to calculate the magnetic stray field for cylindrical geometry (shown in Fig. 9), assuming (for simplicity) homogeneous magnetization. The magnetic field $H(r)$ at a point r [outside the domain = (x, y, z)

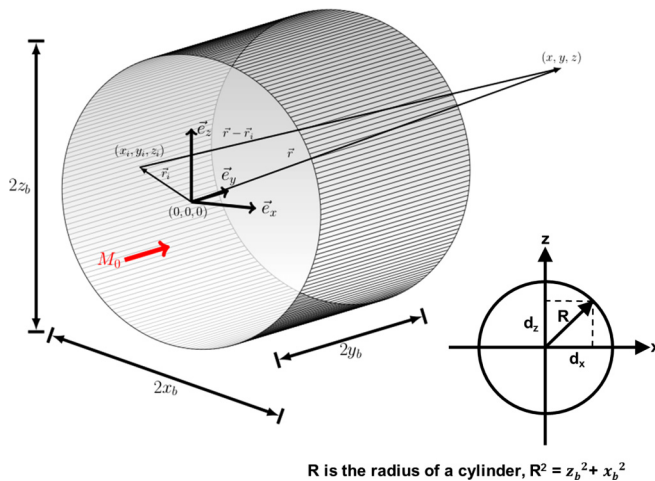


FIG. 9. Pictorial display of cylindrical geometry with integration limits. Magnetization M is shown along the y axis.

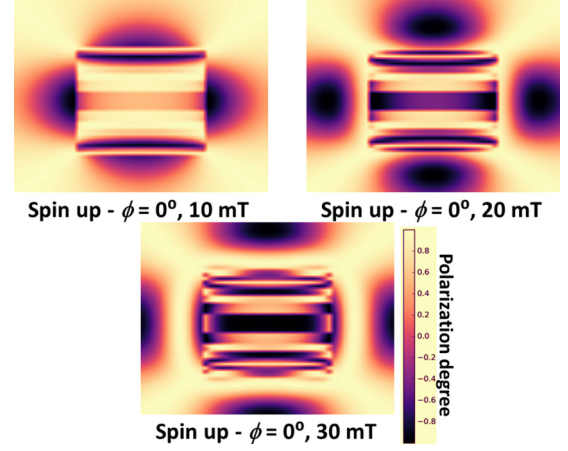


FIG. 10. Calculated flux pinning behavior for different values of external magnetic field for the 0° orientation, compared with Fig. 8 for the single-crystal $\text{La}_{2-x}\text{Sr}_x\text{CuO}_4$ ($x = 0.09$) sample.

with scalar field Φ is described as $\vec{H}(\vec{r}) = -\vec{\nabla}\Phi(\vec{r})$. This results in a Poisson equation with the solution including magnetization and integrating over cylindrical geometry,

$$\Phi(x, y, z) = -\frac{M_o}{4\pi} \frac{\partial}{\partial y} \int_{-y_b}^{y_b} \int_{-\sqrt{R^2-z_b}}^{\sqrt{R^2-z_b}} \int_{-R}^R dy_i dz_i dx_i \times \frac{1}{\sqrt{(x-x_i)^2 + (y-y_i)^2 + (z-z_i)^2}}. \quad (2)$$

Further, the correlated magnetic-field-dependent Larmor spin precession of a polarized neutron beam transmitting through the sample can be theoretically described by semiclassical spin rotation formalism [81–83]. The change in polarization $P(x)$ with respect to the incident polarized $[P(x_0)]$ neutron beam (x is the neutron flight path direction) passing through a homogeneous magnetic field B is given as

$$\frac{\partial \overrightarrow{P}(x)}{\partial x} = A(x)P(x), \quad (3)$$

where

$$A = \frac{\gamma L}{v} \begin{bmatrix} 0 & +B_z & -B_y \\ -B_z & 0 & +B_y \\ +B_y & -B_x & 0 \end{bmatrix} \quad (4)$$

and v is the neutron velocity.

Therefore the change in polarization is given as

$$P(x) = DP(x_0), \quad (5)$$

where the rotation matrix $D = \exp[\int_{x_0}^x dx A(x)]$.

Figure 10 displays (for the 0° sample orientation) the calculated radiographs at various applied magnetic fields, while Fig. 11 shows the corresponding line plots for a clear comparison between calculated and experimentally obtained data at $H_{\text{ext}} = 30$ mT. To calculate the amount of flux pinned inside the sample, the magnitude of the magnetic field that can be pinned inside sample is limited to H_{ext} . Similar features between calculated and experimental data are observed, as shown in Fig. 11. This indicates the possibility of external

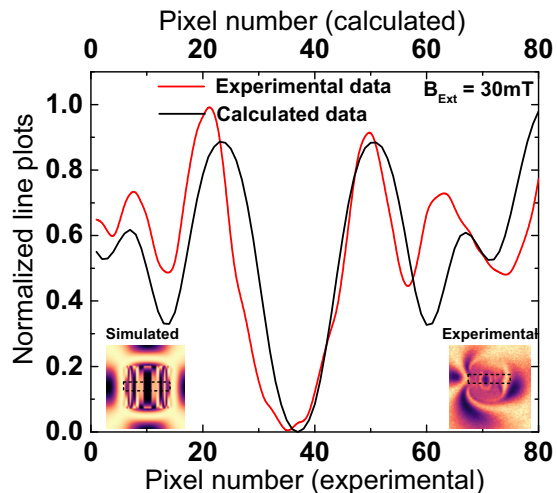


FIG. 11. The normalized line plot (for $H_{\text{ext}} = 30\text{mT}$) showing the comparison between experimental ($T = 5\text{K}$) and calculated radiographs in the 0° orientation for the single-crystal $\text{La}_{2-x}\text{Sr}_x\text{CuO}_4$ ($x = 0.09$) sample. The sum of the transmission intensity for each column as a function of pixel number is plotted. A region of interest selected for this plot is shown in the inset. Each pixel number corresponds to $78\ \mu\text{m}$.

magnetic field completely pinned inside the sample. The calculated radiographs assume an ideal system and conditions, with a 100% degree of polarization, perfect instrument setup, and highly symmetrical and pure cylindrical geometry of the sample. However, in the experimental setup, limited instrument resolution, lower polarization degree (92%), imperfect sample geometry, and therefore inhomogeneity of the pinned magnetic field are expected.

The phase diagram proposed in the literature for the $\text{La}_{2-x}\text{Sr}_x\text{CuO}_4$ series clearly shows the presence of competing superconducting and magnetic interactions as a function of Sr doping and/or the presence of excess oxygen [13,14,84]. Similar behavior is also reported in other high- T_c superconductors [65–69]. The presence of these inhomogeneities can lead to strong and weak vortex pinning centers within the sample. It is possible that at low temperatures the magnetic flux lines pinned to these regions resist the movement. On increasing the temperature (Fig. 5, at 25 K) the pinned magnetic flux begins to disappear from the weak pinning centers first. Eventually, complete disappearance of the pinned magnetic flux (from both strong and weak vortex pinning centers) occurs at T_c . It would be of interest to further explore the distribution of flux pinning over regions of several millimeters (sample size) to visualize regions of high and low densities of pinning centers in high- T_c

superconductors for bulk samples using the polarized neutron imaging technique.

V. CONCLUSION

A polarized neutron imaging study revealed the temperature- and magnetic-field-dependent flux pinning behavior and the Meissner effect of a type-II single-crystal $\text{La}_{2-x}\text{Sr}_x\text{CuO}_4$ ($x = 0.09$) superconductor. We observed signs of the existence of flux pinning behavior down to 5 K. Initially, for $5\text{K} \leq T \leq 15\text{K}$ magnetic fringes with a Gaussian-shaped distribution are visualized, implying pinned flux within the sample. As the temperature is increased to 25 K, nonuniformity in the flux distribution is seen. A further increase in temperature favors a gradual reduction in pinned flux inside the sample, with the sample attaining a normal state above T_c . Additionally, for the Meissner phase with H_{ext} switched on, part of the applied magnetic field is expelled, and part is pinned inside the sample. The flux pinning was further explored as a function of H_{ext} at $T = 5\text{K}$. The evolution of the fringe pattern was observed as a function of H_{ext} . With increasing magnetic field, an increase in the fringe density is ascertained. A comparison between experimentally visualized and calculated pinned magnetic fluxes shows agreeable behavior, with quantification of the pinned magnetic flux inside the bulk of a sample. In addition, the present study demonstrated the potential of the real-space polarized neutron imaging technique for the visualization and quantification of the superconducting mixed state, particularly for high- T_c superconductors.

ACKNOWLEDGMENTS

This material is based upon work supported by the US Department of Energy, Office of Science, Office of Basic Energy Sciences, under Contract No. DE-AC05-00OR22725. We thank Helmholtz-Zentrum Berlin für Materialien und Energie GmbH for the allocation of neutron radiation beam time. This work was supported by the Federal Ministry of Education and Research (BMBF), Project No. 05K10KF1. This manuscript has been authored by UT-Battelle, LLC, under Contract No. DE-AC05-00OR22725 with the US Department of Energy. The US Government retains and the publisher, by accepting the article for publication, acknowledges that the US Government retains a non-exclusive, paid-up, irrevocable, worldwide license to publish or reproduce the published form of this manuscript, or allow others to do so, for US Government purposes. The Department of Energy will provide public access to these results of federally sponsored research in accordance with the DOE Public Access Plan (<http://energy.gov/downloads/doe-public-access-plan>).

- [1] K. A. Müller and J. G. Bednorz, The discovery of a class of high-temperature superconductors, *Science* **237**, 1133 (1987).
- [2] J. M. Tranquada, Neutron scattering studies of antiferromagnetic correlations in cuprates, in *Handbook of High-Temperature Superconductivity*, edited by J. R. Schrieffer and J. S. Brooks (Springer, New York, 2007), pp. 257–298.

- [3] J. Tranquada, Phase separation, charge segregation, and superconductivity in layered cuprates, in *Neutron Scattering in Layered Copper-Oxide Superconductors*, edited by A. Furrer (Kluwer Academic, Dordrecht, 1998), p. 225.
- [4] G. Blatter, M. V. Feigelman, V. B. Geshkenbein, A. I. Larkin, and V. M. Vinokur, Vortices in high-temperature

- superconductors, *Rev. Mod. Phys.* **66**, 1125 (1994), and reference therein.
- [5] C. P. Bean, Magnetization of High-Field Superconductors, *Rev. Mod. Phys.* **36**, 31 (1964).
 - [6] S. A. Kivelson, I. P. Bindloss, E. Fradkin, V. Oganessian, J. M. Tranquada, A. Kapitulnik, and C. Howald, How to detect fluctuating stripes in the high-temperature superconductors, *Rev. Mod. Phys.* **75**, 1201 (2003), and reference therein.
 - [7] J.-M. Tarascon, L. Greene, W. McKinnon, G. Hull, and T. Geballe, Superconductivity at 40 K in the oxygen-defect perovskites $\text{La}_{2-x}\text{Sr}_x\text{CuO}_{4-y}$, *Science* **235**, 1373 (1987).
 - [8] H. Takagi, T. Ido, S. Ishibashi, M. Uota, S. Uchida, and Y. Tokura, Superconductor-to-nonsuperconductor transition in $(\text{La}_{1-x}\text{Sr}_x)_2\text{CuO}_4$ as investigated by transport and magnetic measurements, *Phys. Rev. B* **40**, 2254 (1989).
 - [9] X. Shi, P. V. Lin, T. Sasagawa, V. Dobrosavljević, and D. Popović, Two-stage magnetic-field-tuned superconductor insulator transition in underdoped $\text{La}_{2-x}\text{Sr}_x\text{CuO}_4$, *Nat. Phys.* **10**, 437 (2014).
 - [10] M. Iavarone, S. Moore, J. Fedor, S. Ciocys, G. Karapetrov, J. Pearson, V. Novosad, and S. Bader, Visualizing domain wall and reverse domain superconductivity, *Nat. Commun.* **5**, 4766 (2014).
 - [11] B. Keimer, N. Belk, R. J. Birgeneau, A. Cassanho, C. Y. Chen, M. Greven, M. A. Kastner, A. Aharony, Y. Endoh, R. W. Erwin, and G. Shirane, Magnetic excitations in pure, lightly doped, and weakly metallic La_2CuO_4 , *Phys. Rev. B* **46**, 14034 (1992).
 - [12] M. A. Kastner, R. J. Birgeneau, G. Shirane, and Y. Endoh, Magnetic, transport, and optical properties of monolayer copper oxides, *Rev. Mod. Phys.* **70**, 897 (1998).
 - [13] H. E. Mohottala, B. O. Wells, J. I. Budnick, W. A. Hines, C. Niedermayer, L. Udby, C. Bernhard, A. R. Moodenbaugh, and F.-C. Chou, Phase separation in superoxygenated $\text{La}_{2-x}\text{Sr}_x\text{CuO}_{4+y}$, *Nat. Mater.* **5**, 377 (2006).
 - [14] H. E. Mohottala, B. O. Wells, J. I. Budnick, W. A. Hines, C. Niedermayer, and F. C. Chou, Flux pinning and phase separation in oxygen-rich $\text{La}_{2-x}\text{Sr}_x\text{CuO}_{4+y}$, *Phys. Rev. B* **78**, 064504 (2008).
 - [15] M. P. M. Dean, G. Dellea, R. S. Springell, F. Yakhou-Harris, K. Kummer, N. B. Brookes, X. Liu, Y. J. Sun, J. Strle, T. Schmitt, L. Braicovich, G. Ghiringhelli, I. Božović, and J. P. Hill, Persistence of magnetic excitations in $\text{La}_{2-x}\text{Sr}_x\text{CuO}_4$ from the undoped insulator to the heavily over-doped non-superconducting metal, *Nat. Mater.* **12**, 1019 (2013).
 - [16] A. Gozar, G. Logvenov, L. F. Kourkoutis, A. Bollinger, L. Giannuzzi, D. Muller, and I. Bozovic, High-temperature interface superconductivity between metallic and insulating copper oxides, *Nature (London)* **455**, 782 (2008).
 - [17] A. T. Bollinger, G. Dubuis, J. Yoon, D. Pavuna, J. Misewich, and I. Božović, Superconductor-insulator transition in $\text{La}_{2-x}\text{Sr}_x\text{CuO}_4$ at the pair quantum resistance, *Nature (London)* **472**, 458 (2011).
 - [18] B. Keimer, S. A. Kivelson, M. R. Norman, S. Uchida, and J. Zaanen, From quantum matter to high-temperature superconductivity in copper oxides, *Nature (London)* **518**, 179 (2015).
 - [19] B. O. Wells, Y. S. Lee, M. A. Kastner, R. J. Christianson, R. J. Birgeneau, K. Yamada, Y. Endoh, and G. Shirane, Incommensurate spin fluctuations in high-transition temperature superconductors, *Science* **277**, 1067 (1997).
 - [20] G. S. Boebinger, Y. Ando, A. Passner, T. Kimura, M. Okuya, J. Shimoyama, K. Kishio, K. Tamasaku, N. Ichikawa, and S. Uchida, Insulator-to-Metal Crossover in the Normal State of $\text{La}_{2-x}\text{Sr}_x\text{CuO}_4$ near Optimum Doping, *Phys. Rev. Lett.* **77**, 5417 (1996).
 - [21] W. Buckel and R. Kleiner, *Supraleitung, Grundlagen und Anwendungen*, 7th German edn., Wiley-VCH, Verlag, GmbH, 3, 2012.
 - [22] C. P. Poole, Jr., H. A. Farach, R. J. Creswick, and R. Prozorov, *Superconductivity*, 2nd ed. (Academic, Amsterdam, 2007).
 - [23] J. D. Livingston and W. DeSorbo, *Superconductivity*, edited by R. D. Parks (Dekker, New York, 1969), Vol. 2, p. 1235.
 - [24] M. Tinkham, *Introduction to Superconductivity*, Dover Books of Physics (Dover, New York, 2004).
 - [25] R. P. Huebener, *Magnetic Flux Structures in Superconductors* (Springer, New York, 2001).
 - [26] J. L. MacManus-Driscoll, S. R. Foltyn, Q. X. Jia, H. Wang, A. Serquis, L. Civale, B. Maiorov, M. E. Hawley, M. P. Maley, and D. E. Peterson, Strongly enhanced current densities in superconducting coated conductors of $\text{YBa}_2\text{Cu}_3\text{O}_{7-x} + \text{BaZrO}_3$, *Nat. Mater.* **3**, 439 (2004).
 - [27] T. Haugan, P. N. Barnes, R. Wheeler, F. Meisenkothen, and M. Sumption, Addition of nanoparticle dispersions to enhance flux pinning of the $\text{YBa}_2\text{Cu}_3\text{O}_{7-x}$ superconductor, *Nature (London)* **430**, 867 (2004).
 - [28] A. M. Campbell and D. A. Cardwell, Bulk high temperature superconductors for magnet applications, *Cryogenics* **37**, 567 (1997).
 - [29] R. M. Scanlan, A. P. Malozemoff, and D. C. Larbalestier, Superconducting materials for large scale applications, *Proc. IEEE* **92**, 1639 (2004).
 - [30] J. H. Durrell, A. R. Dennis, J. Jaroszynski, M. D. Ainslie, K. G. B. Palmer, Y.-H. Shi, A. M. Campbell, J. Hull, M. Strasik, E. E. Hellstrom, and D. A. Cardwell, A trapped field of 17.6 T in melt-processed, bulk Gd-Ba-Cu-O reinforced with shrink-fit steel, *Supercond. Sci. Technol.* **27**, 082001 (2014).
 - [31] D. Koelle, R. Kleiner, F. Ludwig, E. Dantsker, and J. Clarke, High-transition-temperature superconducting quantum interference devices, *Rev. Mod. Phys.* **71**, 631 (1999).
 - [32] M. Fujita, H. Hiraka, M. Matsuda, M. Matsuura, J. M. Tranquada, S. Wakimoto, G. Xu, and K. Yamada, Progress in neutron scattering studies of spin excitations in high- T_c cuprates, *J. Phys. Soc. Jpn.* **81**, 011007 (2012), and references therein.
 - [33] L. Udby, N. H. Andersen, F. C. Chou, N. B. Christensen, S. B. Emery, K. Lefmann, J. W. Lynn, H. E. Mohottala, Ch. Niedermayer, and B. O. Wells, Magnetic ordering in electronically phase-separated $\text{La}_{2-x}\text{Sr}_x\text{CuO}_{4+y}$: Neutron diffraction experiments, *Phys. Rev. B* **80**, 014505 (2009).
 - [34] L. Udby, J. Larsen, N. B. Christensen, M. Boehm, Ch. Niedermayer, H. E. Mohottala, T. B. S. Jensen, R. Toft-Petersen, F. C. Chou, N. H. Andersen, K. Lefmann, and B. O. Wells, Measurement of Unique Magnetic and Superconducting Phases in Oxygen-Doped High-Temperature Superconductors $\text{La}_{2-x}\text{Sr}_x\text{CuO}_{4+y}$, *Phys. Rev. Lett.* **111**, 227001 (2013).
 - [35] N. B. Christensen, D. F. McMorro, H. M. Rønnow, B. Lake, S. M. Hayden, G. Aeppli, T. G. Perring, M. Mangkorntong, M. Nohara, and H. Takagi, Dispersive Excitations in the High-Temperature Superconductor $(\text{La}_{1-x}\text{Sr}_x)_2\text{CuO}_4$, *Phys. Rev. Lett.* **93**, 147002 (2004).

- [36] M. Kofu, S.-H. Lee, M. Fujita, H.-J. Kang, H. Eisaki, and K. Yamada, Hidden Quantum Spin-Gap State in the Static Stripe Phase of High-Temperature $\text{La}_{2-x}\text{Sr}_x\text{CuO}_4$ Superconductors, *Phys. Rev. Lett.* **102**, 047001 (2009).
- [37] V. Vignolle, S. M. Hayden, D. F. McMorrow, H. M. Rønnow, B. Lake, C. D. Frost, and T. G. Perring, Two energy scales in the spin excitations of the high-temperature superconductor $\text{La}_{2-x}\text{Sr}_x\text{CuO}_4$, *Nat. Phys.* **3**, 163 (2007).
- [38] T. Suzuki, T. Goto, K. Chiba, T. Shinoda, T. Fukase, H. Kimura, K. Yamada, M. Ohashi, and Y. Yamaguchi, Observation of modulated magnetic long-range order in $\text{La}_{1.88}\text{Sr}_{0.12}\text{CuO}_4$, *Phys. Rev. B* **57**, 3229(R) (1998).
- [39] H. Kimura, K. Hirota, H. Matsushita, K. Yamada, Y. Endoh, S.-H. Lee, C. F. Majkrzak, R. Erwin, G. Shirane, M. Greven, Y. S. Lee, M. A. Kastner, and R. J. Birgeneau, Neutron-scattering study of static antiferromagnetic correlations in $\text{La}_{2-x}\text{Sr}_x\text{Cu}_{1-y}\text{Zn}_y\text{O}_4$, *Phys. Rev. B* **59**, 6517 (1999).
- [40] H. Kimura, H. Matsushita, K. Hirota, Y. Endoh, K. Yamada, G. Shirane, Y. S. Lee, M. A. Kastner, and R. J. Birgeneau, Incommensurate geometry of the elastic magnetic peaks in superconducting $\text{La}_{1.88}\text{Sr}_{0.12}\text{CuO}_4$, *Phys. Rev. B* **61**, 14366 (2000).
- [41] S. Katano, M. Sato, K. Yamada, T. Suzuki, and T. Fukase, Enhancement of static antiferromagnetic correlations by magnetic field in a superconductor $\text{La}_{2-x}\text{Sr}_x\text{CuO}_4$ with $x = 0.12$, *Phys. Rev. B* **62**, 14677(R) (2000).
- [42] S. Wakimoto, G. Shirane, Y. Endoh, K. Hirota, S. Ueki, K. Yamada, R. J. Birgeneau, M. A. Kastner, Y. S. Lee, P. M. Gehring, and S. H. Lee, Observation of incommensurate magnetic correlations at the lower critical concentration for superconductivity in $\text{La}_{2-x}\text{Sr}_x\text{CuO}_4$ ($x = 0.05$), *Phys. Rev. B* **60**, 769(R) (1999).
- [43] S. Wakimoto, R. J. Birgeneau, M. A. Kastner, Y. S. Lee, R. Erwin, P. M. Gehring, S. H. Lee, M. Fujita, K. Yamada, Y. Endoh, K. Hirota, and G. Shirane, Direct observation of a one-dimensional static spin modulation in insulating $\text{La}_{1.95}\text{Sr}_{0.05}\text{CuO}_4$, *Phys. Rev. B* **61**, 3699 (2000).
- [44] M. Matsuda, M. Fujita, K. Yamada, R. J. Birgeneau, M. A. Kastner, H. Hiraka, Y. Endoh, S. Wakimoto, and G. Shirane, Static and dynamic spin correlations in the spin-glass phase of slightly doped $\text{La}_{2-x}\text{Sr}_x\text{CuO}_4$, *Phys. Rev. B* **62**, 9148 (2000).
- [45] S. Wakimoto, R. J. Birgeneau, Y. S. Lee, and G. Shirane, Hole concentration dependence of the magnetic moment in superconducting and insulating $\text{La}_{2-x}\text{Sr}_x\text{CuO}_4$, *Phys. Rev. B* **63**, 172501 (2001).
- [46] M. Fujita, K. Yamada, H. Hiraka, P. M. Gehring, S. H. Lee, S. Wakimoto, and G. Shirane, Static magnetic correlations near the insulating-superconducting phase boundary in $\text{La}_{2-x}\text{Sr}_x\text{CuO}_4$, *Phys. Rev. B* **65**, 064505 (2002).
- [47] B. Lake, H. M. Rønnow, N. B. Christensen, G. Aeppli, K. Lefmann, D. F. McMorrow, P. Vorderwisch, P. Smeibidl, N. Mangkorntong, T. Sasagawa, M. Nohara, H. Takagi, and T. E. Mason, Antiferromagnetic order induced by an applied magnetic field in a high-temperature superconductor, *Nature (London)* **415**, 299 (2002).
- [48] T. Reimann, S. Mühlbauer, M. Schulz, B. Betz, A. Kaestner, V. Pipich, P. Böni, and C. Grünzweig, Visualizing the morphology of vortex lattice domains in a bulk type-II superconductor, *Nat. Commun.* **6**, 8813 (2015).
- [49] S. Mühlbauer, C. Pfleiderer, P. Böni, M. Laver, E. M. Forgan, D. Fort, U. Keiderling, and G. Behr, Morphology of the Superconducting Vortex Lattice in Ultrapure Niobium, *Phys. Rev. Lett.* **102**, 136408 (2009).
- [50] M. Laver, C. J. Howell, E. M. Forgan, A. B. Abrahamsen, D. Fort, C. D. Dewhurst, S. Mühlbauer, D. K. Christen, J. Kohlbrecher, R. Cubitt, and S. Ramos, Structure and degeneracy of vortex lattice domains in pure superconducting niobium: A small-angle neutron scattering study, *Phys. Rev. B* **79**, 014518 (2009).
- [51] S. Mühlbauer, C. Pfleiderer, P. Böni, E. M. Forgan, E. H. Brandt, A. Wiedenmann, U. Keiderling, and G. Behr, Time resolved stroboscopic neutron scattering of vortex lattice dynamics in superconducting niobium, *Phys. Rev. B* **83**, 184502 (2011).
- [52] A. Pautrat and A. Brület, Temperature dependence of clusters with attracting vortices in superconducting niobium studied by neutron scattering, *J. Phys. Condens. Matter* **26**, 232201 (2014).
- [53] D. K. Christen, F. Tasset, S. Spooner, and H. A. Mook, Study of the intermediate mixed state of niobium by small-angle neutron scattering, *Phys. Rev. B* **15**, 4506 (1977).
- [54] S. J. Bending, Local magnetic probes of superconductors, *Adv. Phys.* **48**, 449 (1999).
- [55] I. Zeljkovic, E. J. Main, T. L. Williams, M. C. Boyer, K. Chatterjee, W. D. Wise, Y. Yin, M. Zech, A. Pivonka, T. Kondo, T. Takeuchi, H. Ikuta, J. Wen, Z. Xu, G. D. Gu, E. W. Hudson, and J. E. Hoffman, Scanning tunneling microscopy imaging of symmetry-breaking structural distortion in the bismuth-based cuprate superconductors, *Nat. Mater.* **11**, 585 (2012).
- [56] J. R. Kirtley, Fundamental studies of superconductors using scanning magnetic imaging, *Rep. Prog. Phys.* **73**, 126501 (2010), and reference therein.
- [57] Ø. Fischer, M. Kugler, I. Maggio-Aprile, C. Berthod, and C. Renner, Scanning tunneling spectroscopy of high-temperature superconductors, *Rev. Mod. Phys.* **79**, 353 (2007).
- [58] H. Suderow, I. Guillamón, J. G. Rodrigo, and S. Vieira, Imaging superconducting vortex cores and lattices with a scanning tunneling microscope, *Supercond. Sci. Technol.* **27**, 063001 (2014).
- [59] J. E. Hoffman, Spectroscopic scanning tunneling microscopy insights into Fe-based superconductors, *Rep. Prog. Phys.* **74**, 124513 (2011).
- [60] C. Jooss, J. Albrecht, H. Kuhn, S. Leonhardt, and H. Kronmüller, Magneto-optical studies of current distributions in high- T_C superconductors, *Rep. Prog. Phys.* **65**, 651 (2002), and references therein.
- [61] R. Prozorov, R. W. Giannetta, A. A. Polyanskii, and G. K. Perkins, Topological hysteresis in the intermediate state of type-I superconductors, *Phys. Rev. B* **72**, 212508 (2005).
- [62] R. Prozorov, Equilibrium Topology of the Intermediate State in Type-I Superconductors of Different Shapes, *Phys. Rev. Lett.* **98**, 257001 (2007).
- [63] R. Prozorov, A. F. Fidler, J. R. Hoberg, and P. C. Canfield, Suprafroth in type-I superconductors, *Nat. Phys.* **4**, 327 (2008).
- [64] A. Finkler, D. Vasyukov, Y. Segev, L. Néeman, E. O. Lachman, M. L. Rappaport, Y. Myasoedov, E. Zeldov, and M. E. Huber, Scanning superconducting quantum interference device on a tip for magnetic imaging of nanoscale phenomena, *Rev. Sci. Instrum.* **83**, 073702 (2012).
- [65] K. Harada, O. Kamimura, H. Kasai, T. Matsuda, A. Tonomura, and V. V. Moshchalkov, Observation of dynamic interaction of

- vortices with pinning centers by lorentz microscopy, *Science* **271**, 1393 (1996).
- [66] A. Tonomura, H. Kasai, O. Kamimura, T. Matsuda, K. Harada, J. Shimoyama, K. Kishio, and K. Kitazawa, Motion of vortices in superconductors, *Nature (London)* **397**, 308 (1999).
- [67] A. Tonomura, H. Kasai, O. Kamimura, T. Matsuda, K. Harada, T. Yoshida, T. Akashi, J. Shimoyama, K. Kishio, T. Hanaguri, K. Kitazawa, T. Masui, S. Tajima, N. Koshizuka, P. L. Gammel, D. Bishop, M. Sasase, and S. Okayasu, Observation of Structures of Chain Vortices Inside Anisotropic High- T_c Superconductors, *Phys. Rev. Lett.* **88**, 237001 (2002).
- [68] K. Harada, T. Matsuda, J. Bonevich, M. Igarashi, S. Kondo, G. Pozzi, U. Kawabe, and A. Tonomura, Real-time observation of vortex lattices in a superconductor by electron microscopy, *Nature (London)* **360**, 51 (1992).
- [69] K. Harada, Lorentz microscopy observation of vortices in high- T_c superconductors using a 1-MV field emission transmission electron microscope, *Microscopy* **62** (Suppl. 1), S3 (2013).
- [70] W. Treimer, Radiography and tomography with polarized neutrons, *J. Magn. Magn. Mater.* **350**, 188 (2014).
- [71] K. Kishio, Y. Nakayama, N. Motohira, T. Noda, T. Kobayashi, K. Kitazawa, K. Yamafuji, I. Tanaka, and H. Kojima, Anisotropic magnetization, flux pinning and critical current density of La-Sr-Cu-O single crystal, *Supercond. Sci. Technol.* **5**, S69 (1992).
- [72] N. Kardjilov, I. Manke, M. Strobl, A. Hilger, W. Treimer, M. Meissner, T. Krist, and J. Banhart, Three-dimensional imaging of magnetic fields with polarized neutrons, *Nat. Phys.* **4**, 399 (2008).
- [73] M. Dawson, I. Manke, N. Kardjilov, A. Hilger, M. Strobl, and J. Banhart, Imaging with polarized neutrons, *New J. Phys.* **11**, 043013 (2009).
- [74] M. Schulz, A. Neubauer, P. Böni, and C. Pfleiderer, Neutron depolarization imaging of the hydrostatic pressure dependence of inhomogeneous ferromagnets, *Appl. Phys. Lett.* **108**, 202402 (2016).
- [75] A. S. Tremsin, N. Kardjilov, M. Strobl, I. Manke, M. Dawson, J. B. McPhate, J. V. Vallerga, O. H. W. Siegmund, and W. B. Feller, Imaging of dynamic magnetic fields with spin-polarized neutron beams, *New J. Phys.* **17**, 043047 (2015).
- [76] W. Treimer, O. Ebrahimi, N. Karakas, and R. Prozorov, Polarized neutron imaging and three-dimensional calculation of magnetic flux trapping in bulk of superconductors, *Phys. Rev. B* **85**, 184522 (2012).
- [77] I. Dhiman, O. Ebrahimi, N. Karakas, H. Hoppner, R. Ziesche, and W. Treimer, Role of temperature on flux trap behavior in $\langle 100 \rangle$ Pb cylindrical sample: Polarized neutron radiography investigation, *Phys. Proc.* **69**, 420 (2015).
- [78] W. Treimer, O. Ebrahimi, N. Karakas, and S. O. Seidel, PONTON - An instrument for imaging with polarized neutrons, *Nucl. Instrum. Methods Phys. Res., Sect. A* **651**, 53 (2011).
- [79] E. H. Brandt, Geometric barrier of superconductors with and without pinning, *Phys. B (Amsterdam, Neth.)* **284-288**, 743 (2000).
- [80] R. Engel-Herbert and T. Hesjedal, Calculation of the magnetic stray field of a uniaxial magnetic domain, *J. Appl. Phys.* **97**, 074504 (2005).
- [81] H. Leeb, M. Hochhold, G. Badurek, R. J. Buchelt, and A. Schrickler, Neutron magnetic tomography: A feasibility study, *Aust. J. Phys.* **51**, 401 (1998).
- [82] G. Badurek, M. Hochhold, and H. Leeb, Neutron magnetic tomography—A novel technique, *Phys. B (Amsterdam, Neth.)* **234-236**, 1171 (1997).
- [83] M. Th. Rekveldt, Study of ferromagnetic bulk domains by neutron depolarization in three dimensions, *Z. Phys.* **259**, 391 (1973); Correlations in ferromagnetic domain structures studied by means of the neutron depolarization technique, *J. Magn. Magn. Mater.* **1**, 342 (1976).
- [84] M. Terasawa, N. Takezawa, K. Fukushima, T. Mitamura, X. Fan, H. Tsubakino, T. Kohara, K. Ueda, Y. Awaya, T. Kambara, M. Matsuda, and G. Tatara, Flux pinning and flux creep in $\text{La}_{2-x}\text{Sr}_x\text{CuO}_4$ with splayed columnar defects, *Phys. C (Amsterdam, Neth.)* **296**, 57 (1998).